Available online at www.sciencedirect.com
ScienceDirect
International Journal of Heat and Fluid Flow 27 (2006) 1043–1053
International Journal of HEAT AND FLUID FLOW
www.elsevier.com/locate/ijhff

Computational and experimental study of annular photo-reactor hydrodynamics

D. Angelo Sozzi, Fariborz Taghipour *

University of British Columbia, Department of Chemical and Biological Engineering, 2360 East Mall, Vancouver, B.C., Canada V6T 1Z3

Received 26 July 2005; accepted 19 January 2006
Available online 20 March 2006

Abstract

The performance of ultraviolet (UV) reactors used for water treatment is greatly influenced by the reactor hydrodynamics due to the non-homogeneity of the radiation field. Reliable modeling of the reactor flow structures is therefore crucial for the design process. In this study, the turbulent flow through two characteristic annular UV-reactor configurations, with inlets concentric (L-shape) and normal (U-shape) to the reactor axis, was investigated through computational fluid dynamic (CFD). The modeling results were evaluated with the velocity profiles from particle image velocimetry (PIV) experiments. The influence of mesh structure and density, as well as three turbulence models: Standard κ–ϵ, Realizable κ–ϵ, and Reynolds stress model (RSM), on the simulation results were evaluated. Mesh-independent solutions were achieved at mean cell volumes of 5×10^{-9} m^3. The Realizable κ–ϵ displayed the best overall match to the experimental PIV measurements. In general, the CFD models showed a close agreement with the experimental data for the majority of the reactor domain and captured the influences of reactor configuration and internal reactor structures on the flow distribution. The validated CFD hydrodynamic models could be integrated with kinetic and radiation distribution models for UV-reactor performance simulation.

Keywords: CFD; PIV; Annular reactor hydrodynamics; Mesh dependency; Turbulence models

1. Introduction

Water treatment processes using UV technology have seen a rapid growth in recent years. UV Photolysis and photo-initiated oxidation have great potentials for the inactivation of microorganisms and the destruction of a wide range of contaminants in water.

A successful fundamental simulation of UV systems is the basis for several applications: virtual prototyping, cost effective design optimization, and on-line control and performance evaluation. UV reactor simulation can be achieved by considering the rate of reaction linked to the non-homogeneous UV-radiation power through the local volumetric rate of energy absorption. This spatial dependency makes a three-dimensional resolution of the reaction rate indispensable (Kamimura et al., 2002). Only after computing the full hydrodynamic flow of the reactor does it become possible to correctly model the reaction rate inside UV reactors. The effect of the interaction between reactor hydrodynamics and local radiation intensity on the concentration distribution of contaminants in UV-advanced oxidation reactors was shown by Pareek et al. (2003). Schoenen et al. (1993) demonstrated the influence of the flow field and geometry on the performance of disinfection systems.

Realizing the importance of an integrated model, Romero et al. (1983) set up the fundamental balances needed to solve the mass, momentum, energy, and chemical reaction rate equations for annular UV reactors. Because of a lack of computing power, they assumed axial symmetry and implemented a simplified set of equations for two-dimensional geometries, a method that was then applied

* Corresponding author. Fax: +1 604 822 6003.
E-mail addresses: angelo@sozzi.ch (D.A. Sozzi), fariborz@chml.ubc.ca (F. Taghipour).

0142-727X/$ - see front matter © 2006 Elsevier Inc. All rights reserved.
doi:10.1016/j.ijheatfluidflow.2006.01.006

for subsequent studies of different geometries and reaction kinetics by Cassano et al. (1995). With the increased performance of computational resources and the development of simulation software, computational fluid dynamics (CFD) is becoming an affordable engineering tool to simulate and optimize reactor designs. The viability of CFD for the design and optimization of chemical reactors has been demonstrated for a variety of systems (Hjertager et al., 2002; Marchisio and Barresi, 2003). CFD has been applied to the simulation of UV-reactor hydrodynamics (Janex et al., 1998; Wright and Hargreaves, 2001). It has also been utilized to simulate UV-reactor performance through the integration of reactor hydrodynamics, radiation distribution, and UV-reaction kinetics (Kamimura et al., 2002; Pareek et al., 2003; Unluturk et al., 2004). CFD prediction of two-dimensional turbulent flow in the central region of an open channel UV reactor was compared with the experimental flow measurements using laser Doppler velocimetry and good agreement was reported in some aspects (Lyn et al., 1999).

While CFD is becoming a mainstream modeling tool, anticipating the flow characteristics and selecting the appropriate modeling technologies (boundary conditions, turbulence model, etc.) remain the responsibility of the user. As CFD is based on the governing equations of mass and momentum conservation as well as mathematical models with simplifying assumptions, there are many possible sources for errors, and validation of the CFD results is vital for the effective use of such a model. Advanced experimental methods such as laser Doppler velocimetry (LDV) and particle image velocimetry (PIV) have been shown to give detailed information on the turbulent flow field in stirred vessels (Meyers et al., 1997; Ranade et al., 2001) and in tubular channels (Escudier and Smith, 1999; Pruvost et al., 2000; Hu et al., 2000).

CFD solves the governing equations of the flow mass and momentum conservation in the discretised computational domain using a numerical (e.g. finite volume) method. Different approaches can be taken for modeling turbulent flows. In the Reynolds averaged Navier–Stokes (RANS) approach, instantaneous velocity components are usually divided into their mean and fluctuating values ($u = \overline{u} + u'$). The mass and momentum conservation in suffix notation are

$$\frac{\partial \overline{u_i}}{\partial x_i} = 0 \tag{1}$$

$$\frac{\partial \overline{u_i}}{\partial t} + u_j \frac{\partial \overline{u_i}}{\partial x_j} = -\frac{1}{\rho}\frac{\partial p}{\partial x_i} + \frac{\partial}{\partial x_j}\left(\mu \frac{\partial \overline{u_i}}{\partial x_j} - \overline{u_i' u_j'}\right) \quad i, j = 1, 2, 3 \text{ (for } x,\ y,\ z) \tag{2}$$

where ρ is the density, p the pressure, μ the viscosity, u_i the instantaneous velocity, $\overline{u_i}$ the mean velocity, and u_i' the fluctuating velocity component in the ith direction. The unknown terms $-\rho\overline{u_i' u_j'}$, called the Reynolds stresses, represent the effect of small-scale turbulence on the mean flow and need to be closed by using one of the turbulence models.

Among the factors that may influence the CFD results are the discretisation of the domain (structure and size of the cells), and the type of modeling approach employed (turbulence model, etc). Grid generation is one of the most important parts of CFD analysis. The quality of the grid has a direct influence on the quality of the analysis, regardless of the flow solver used. Additionally, the solver will be more robust and efficient when using a well-constructed mesh. A quality grid, capable of representing the geometry, is the basis for a reliable, accurate simulation. In general, both mesh quality and grid independence of the solution need to be ensured (Douglas et al., 2002).

When the flow is within the turbulent regime (typically the case in UV reactors), additional models are required to consider the effect of turbulent fluctuations on the flow. For most engineering applications, only the mean effect of turbulent quantities is important; therefore, the time-averaged flow properties are of interest. The RANS equations are the established averaging approach for modeling turbulence. Two classes of RANS turbulence models are the κ–ϵ models and the Reynolds stress model (RSM), each relying on a set of implied assumptions with relative advantages and disadvantages. The κ–ϵ models use the Boussinesq hypothesis to relate the Reynolds stresses to the mean velocity gradient through the turbulent kinetic energy κ and the turbulent dissipation rate ϵ. This implies locally isotropic turbulent fluctuations and a local equilibrium of the production and dissipation terms. Primary shear stresses are predicted well with these two-equation models, but secondary shear stresses and normal stresses are not.

The Standard κ–ϵ model (Launder and Spalding, 1972) is the simplest of the two-equation models. It is robust, economic, and predicts a wide range of flows reasonably well. But the assumptions are only valid in fully turbulent flows; it cannot deal well with complex three-dimensional flows, sudden changes in the mean strain rate, curved surfaces, secondary motions, and flow separation. It tends to overpredict turbulence generation in areas where the mean flow is highly accelerated or decelerated (Hinze, 1975).

The Realizable κ–ϵ model (Shih et al., 1995) incorporates time scale realizability and an additional source term in the epsilon equation for improved performance in flows involving adverse pressure gradients (including separated flows). It also features a realizability constraint on the predicted stress tensor. This avoids excessive levels of turbulence generation in regions of large mean strain, such as occur in impinging flows.

The RSM model (Launder et al., 1975) uses the exact transport equations for Reynolds stresses, closing the unknown correlations at this level (second-order closure model). It abandons the isotropic eddy-viscosity hypothesis and performs well for many complex flows (e.g. highly swirling flows). The seven additional partial differential equations (PDEs) and a tendency to require a finer mesh make it computationally more expensive. Table 1 provides a brief summary of the advantages and disadvantages of the κ–ϵ and Reynolds stress models.

Table 1
Comparison of κ–ϵ turbulence models and RSM-model. Several sources contributed to this table (Ranade, 2002; Jaw and Chen, 1998; Rodi, 1979; Fluent, 2003)

Model	Advantages	Disadvantages
Standard κ–ϵ	• Simplest model to represent variation of turbulence length and velocity scales • Robust and economical • Good performance in many industrial flows • Most widely validated model	• Assumes isotropic eddy viscosity • Performs poorly for – unconfined flows – rotating flows – non-circular ducts – curved boundary layers
Realizable κ–ϵ	• Compensates for large strain rates and streamline curvature • Resolves round-jet anomaly • Better for impinging and separating flows	• Assumes isotropic eddy viscosity • Not sufficiently validated
RSM	• Most general model of all classical turbulence models • Performs well for complex flows including non-circular ducts and curved flows • Resolves swirling flows	• Computationally expensive (+7 PDEs) • Sometimes as poor as κ–ϵ due to problems with ϵ equation • Prone to convergence difficulties • Not widely validated

Despite a number of studies on CFD modeling of UV reactor hydrodynamics, and the development of integrated CFD models for UV reactor performance, to the authors' knowledge there have been no efforts reported in the open literature to validate the CFD simulations with experimentally obtained flow field information using PIV. Also, little if any information can be found on the effect of computational domain discretisation and turbulence models on the CFD results. The objective of this work was to carry out a comprehensive CFD study of the turbulent flow occurring in annular UV reactors and to compare the results with experimental measurements. The cylindrical UV reactor with a concentric lamp parallel to the reactor body, which represents the basic design for many current small and medium UV reactors, was investigated. The effect of grid number and structure on the CFD results in two commonly used UV-reactor geometries, with an inlet parallel (L-shape) and normal (U-shape) to the main reactor body, were studied. The influence of three different turbulence models was also assessed for both geometries. The results were evaluated by comparison with experimental data obtained from particle image velocimetry (PIV).

2. CFD modeling

The two model UV-reactor geometries studied, the L-shape and U-shape shown in Fig. 1, are based on the existing industrial reactors as currently used. The simulation results were compared to the experimental PIV results from Plexiglas prototypes having the same dimensions. Both shapes shared the same main reaction tube diameter of 8.9 cm (3.5 in.), length of 88.9 cm (35 in.), with a central UV lamp of 2 cm (0.79 in.) in diameter. The inlet and outlet ports, with a diameter of 1.91 cm (0.75 in.), were placed 2.54 cm (1 in.) from each respective end for the U-shape, while the L-shape inlet was centered on the front plate. The inlet tube length with an $\frac{L_1}{D_1} = 45$ was chosen to ensure that a fully developed flow was established at the entrance

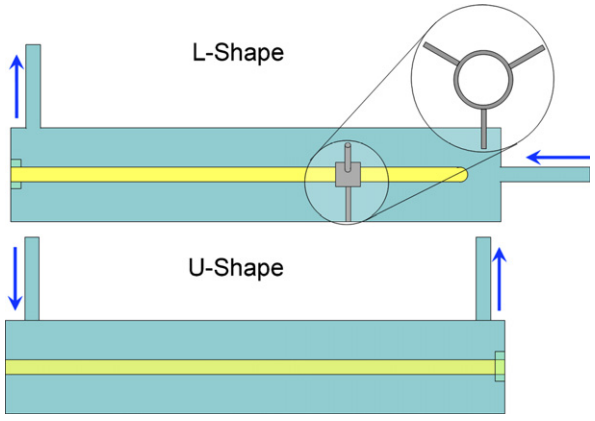

Fig. 1. Schematic diagram of the L- and U-shape reactors. The inlets and outlets are indicated by arrows. The lamp holder in the L-shape is enlarged.

of the reactor. A volumetric inlet rate of 6.94×10^{-4} m^3/s (11 GPM), corresponding to a mean inlet velocity of 2.43 m/s, a mean axial velocity in the reactor of 0.11 m/s, and a Reynolds number of 10,000 in the reactor annulus was set.

The commercial mesh generator GAMBIT was used to create the grid and the tgrid tool was employed to merge separately meshed domains. The inlet and outlet tubes were meshed with 5000–8000 structured (Cooper) cells in all cases. Both structured and unstructured cells were employed to discretise the main reactor domain (Fig. 2). For the unstructured tetrahedral mesh, no subdomains were needed. The size of cells was defined by cell volume and refined manually if necessary. For the structured mesh, the domain was split into several subdomains reducing the use of unstructured cells to the volume containing the lamp holder in the L-shape reactor. For the U-shape, the inlet volume and lamp region with high velocity gradients, round-jet impingement, and flow separation required a higher mesh resolution, while the lamp tip and

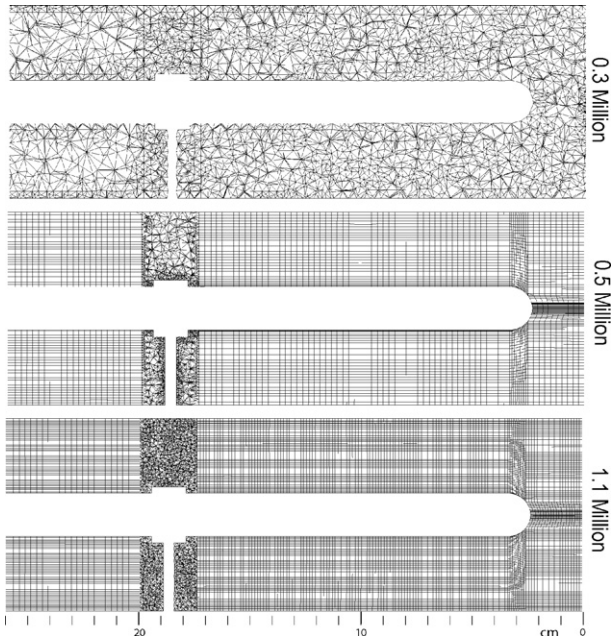

Fig. 2. Meshes used in L-shape reactor. From the top to the bottom there are: Fully unstructured, structured with low mesh density and structured with high mesh density. The lamp holder region could not be meshed with structured cells and remained unstructured.

the lamp holder needed more attention in the case of the L-shape.

A commercial CFD software package, Fluent (V6.1.22), was used to solve the conservation of mass and momentum equations for the described geometries. The internal structures were reproduced as 3D volumes and a no-slip boundary condition was imposed on the reactor walls. The operating fluid was defined as water at 293 K. Velocity inlets, with a hydraulic diameter of 1.91 cm, 10% turbulent intensity, and a uniform velocity distribution were defined and a fully developed flow (outflow) was applied at the exit. In all cases, the standard log law wall functions were employed. The segregated steady-state solver was used to iterate the solutions, starting with a first order upwind discretisation scheme, and continuing with the second-order upwind scheme for the final converged solution. The SIMPLE method was chosen for the pressure–velocity coupling. Convergence of the numerical solution was ensured by monitoring the scaled residuals of continuity, x, y, z-velocities, and the turbulence parameters to a criterion of less than 10^{-5}. In addition, the velocity magnitude at two points defined in areas with high velocity gradients were used as indicators.

The importance of correctly resolving the turbulent flow behavior for chemical reactors has been stressed. The exact Navier–Stokes equations are replaced by Reynolds averaged equations generating the need for closure models to obtain solutions. However, no turbulence model is universal and the choice is based on considerations of domain geometry and the anticipated flow behavior. Three turbulence models, the Standard κ–ϵ model, the Realizable κ–ϵ model, and the Reynolds Stress Model (RSM) were selected, based on availability (most widely used models) and usability (average time and computing power needed).

3. PIV experiments

The CFD flow simulations were validated using experimental PIV results. PIV is a non-intrusive method of instantaneous flow field visualization. A sheet of laser light flash illuminates particles in the flow field and a digital camera captures the two points in time. The resulting flow velocity extracted from this digital image pair is an instantaneous snapshot of the flow in the area viewed.

The particle images were recorded using an 80C60 HiSense PIV camera connected to a FlowMap System Hub (Dantec Dynamics Inc.) for synchronization. A New-Wave Solo-15 laser system provided illumination of the particles. The seeding (PSP, 20 μm diameter, 1.03 g/cm^3) was adjusted to 5–10 particles per interrogation window. The image data were analyzed with a multi-pass adaptive cross-correlation technique with interrogation windows of 32×32 pixels and an overlap of 50% on the final pass. For each measurement, 250–500 image pairs were used and the vector statistical average was calculated to obtain a time-averaged flow field. The PIV experiments were performed in exact full scale Plexiglas replications of the investigated reactors with internal components including the quartz lamp sleeve and lamp holder. The reactors were placed within a Plexiglas tank that was filled with distilled water, to eliminate optical distortion caused by the curved external surface of the reactors. The accuracy of the PIV velocity measurements was determined through statistical analysis over the 250 instantaneous vector fields at several points. Small errors (95% confidence interval) of <1% were observed for the high velocities at the inlet. The relative errors were determined to be <5% for the intermediate flow

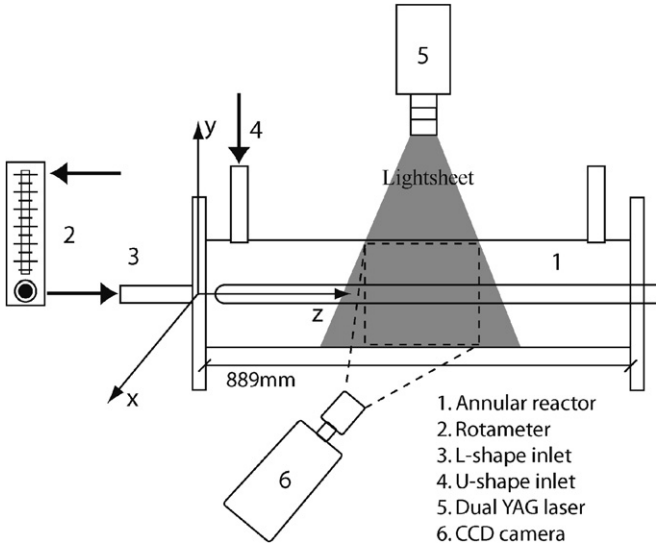

Fig. 3. Schematic diagram of the experimental setup and PIV system. Inlet and outlets of the L- and U-shape reactors are indicated by arrows.

rates located 10 cm from the reactor inlet, and <17% for the low axial flow speeds at distances of 23 cm and beyond. The schematic diagram of the PIV experimental setup is provided in Fig. 3. The details of the PIV experimental measurements are discussed elsewhere (Sozzi and Taghipour, 2005).

4. Results and discussion

In annular U- and L-shape reactors (Fig. 1), a typical structure is found to occur at the inlet where the round inlet jet impinges on the central annulus, from the front for the L-shape, or from the top for the U-shape reactor. The cylindrical annulus poses several challenges, such as flow separation, flow attachment/detachment, and also introduces an element of unsteadiness. The flow around bluff bodies is known to show a time-dependent structure in the near wake, called vortex shedding. Since the flow is turbulent but statistically steady state, the RANS turbulence modeling approach remains a viable approximation. However, the discretisation of this volume and the choice of RANS model may have a large influence on the final results. The effects of discretisation method and turbulence modeling on the CFD results are presented separately for the L-shape and U-shape reactors.

4.1. L-shape reactor

4.1.1. Influence of grid structure

The influence of the finite volume mesh on the CFD results was studied for both structured and unstructured grids. While an unstructured mesh is easier to generate initially and often the only solution for complex geometries, the unstructured tetrahedral elements are not considered ideal from an accuracy point of view (Chow et al., 1996). Control over the number and distribution of cells generated is restricted, resulting in higher cell densities compared to a structured grid. Three test cases for the L-shape reactor are presented in Fig. 2, an unstructured mesh with 0.3 million cells, and two structured meshes with 0.5 and 1.1 million cells. The central lamp with a rounded tip close to the entrance is held in place by a lamp holder at 18.6 cm (7.3 in.). The three pronged lamp holder, required to center and retain the lamp at the entrance of L-shape reactors, was discretised with tetrahedral cells in all cases since no structured mesh was possible. The more precise control over the structured mesh is evident at the inlet and the lamp tip.

The simulated vectors of velocity magnitude of the flow produced in the reactor using the Realizable κ–ϵ turbulence model are presented on the center-plane of the reactor in Fig. 4. The axisymmetric inlet jet entering the reactor from the right impinges on the lamp tip, separates and expands toward the outer walls. The expanding jet creates a pressure gradient leading to a region of flow recirculation along the reactor wall, and finally merges with the outer boundaries shortly after the lamp holder.

Even though the three plots show similar flow patterns, the disparity between the unstructured and structured meshes is easily visible and especially prominent when comparing the centers of recirculation. With a denser unstructured mesh, velocity profiles with a closer match to those obtained from structured mesh were achieved, but the results remained disparate within the memory dictated

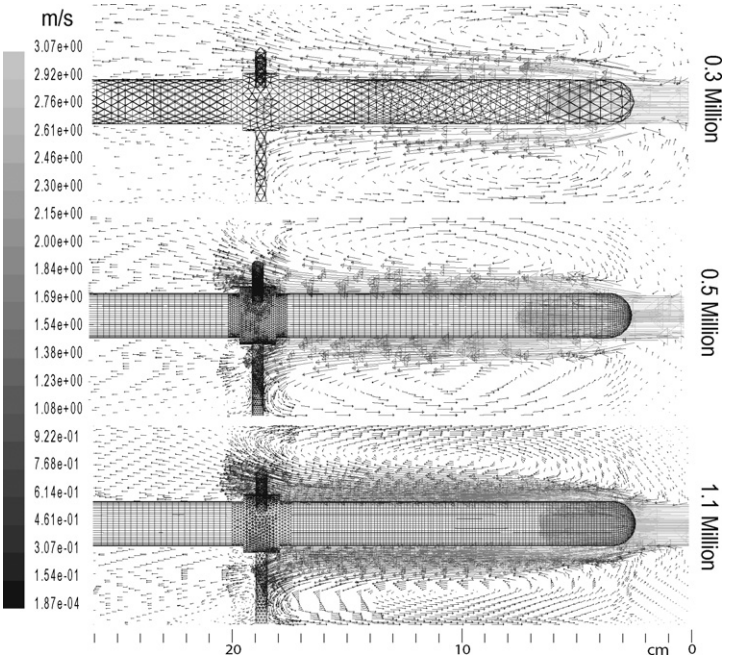

Fig. 4. Vectors of velocity magnitude in the L-shape reactor. Results were obtained using the Realizable κ–ϵ turbulence model and the meshes described in Fig. 2 (only every fourth velocity vector is shown).

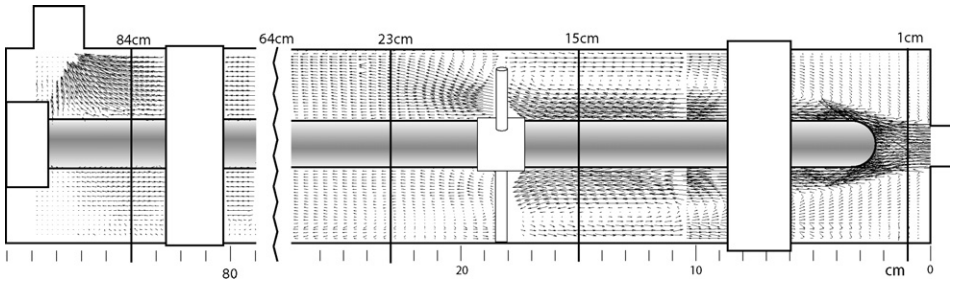

Fig. 5. Vectors of velocity magnitude from PIV experimental data at center plane of L-shape reactor. Positions used for quantitative comparison are shown as vertical lines at different distances from the reactor inlet (see Fig. 7).

limits of a maximal 1.2 million cells. It can be concluded that a combination of unstructured mesh and lower mesh number were the reason for this difference. The two structured mesh plots show very good agreement and no difference between the low and high mesh is discernible, aside from the higher resolution.

Comparing the results to PIV data (Fig. 5) shows that the CFD model yields flow patterns that are in good qualitative agreement for all mesh structures. However, some differences can be noted when comparing the structured and unstructured meshes. The centers of the primary recirculation loops are situated further along the reactor z-axis for the structured meshes, and the loops are elongated, which agrees well with the PIV data. In the area just behind the lower spoke of the lamp holder, the structured mesh solutions show a small recirculation loop that also shows up in the experimental data. There are no major flow structures that have not been captured by the CFD solutions.

Fig. 6a and b compares the CFD results obtained using the three grid structures at positions 1 and 15 cm from the reactor entrance with the PIV experimental results. At these distances, the influence of turbulence is not significant and differences are primarily mesh related. The maximum inlet velocity of 2.8 m/s and the overall velocity profiles are closely matched by all the CFD results. The unstructured mesh results, however, show a deviation from both the structured mesh results and the experimental data. The difference is especially notable at 15 cm and is a direct result of the shifted primary recirculation loop predictions. Both structured meshes show little deviation from each other and continue to match the experimental values closely. From these observations, it can be assumed that 0.5 million structured cells or more are sufficient for a mesh independent solution of UV reactors with comparable dimensions, geometry, and flow rate.

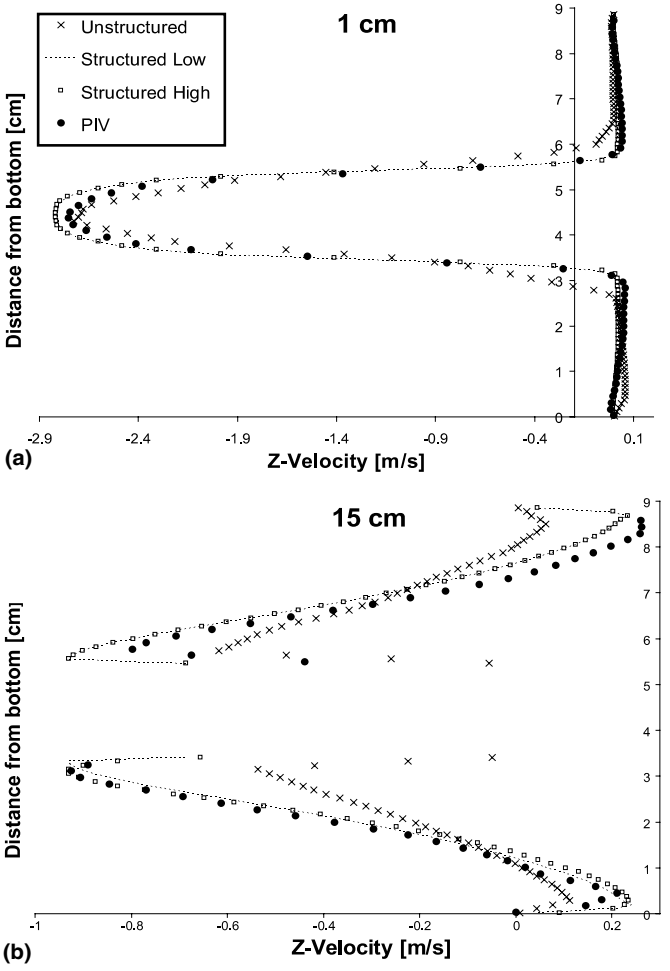

Fig. 6. Quantitative comparison of the (axial) z-velocity component obtained using the three mesh structures give in Fig. 2. Data are extracted from CFD and PIV results (Fig. 4) at positions 1 and 15 cm from the reactor inlet (Fig. 5).

4.1.2. Comparison of turbulence models

The effect of turbulence models was investigated using the structured mesh with 0.5 million cells for the Standard κ–ϵ, the Realizable κ–ϵ, and the Reynolds Stress models. A comparison of the z-velocity components (along the reactor axis) obtained using all three turbulence models with experimental PIV data at 1, 15, 23, 38, 64 and 83 cm from the reactor inlet is shown in Fig. 7. At 1 cm, in the region of the free inlet jet, all turbulence models show an excellent match with each other and the experimental data. It can be noted that the Standard κ–ϵ model shows some difficulty matching the outer regions of the free round inlet jet. At 15 cm, in Fig. 7, both the RSM and Realizable κ–ϵ models provide an excellent match of both flow contours and velocity, while the Standard κ–ϵ model under-predicts the returning flow velocity at the reactor walls indicating that

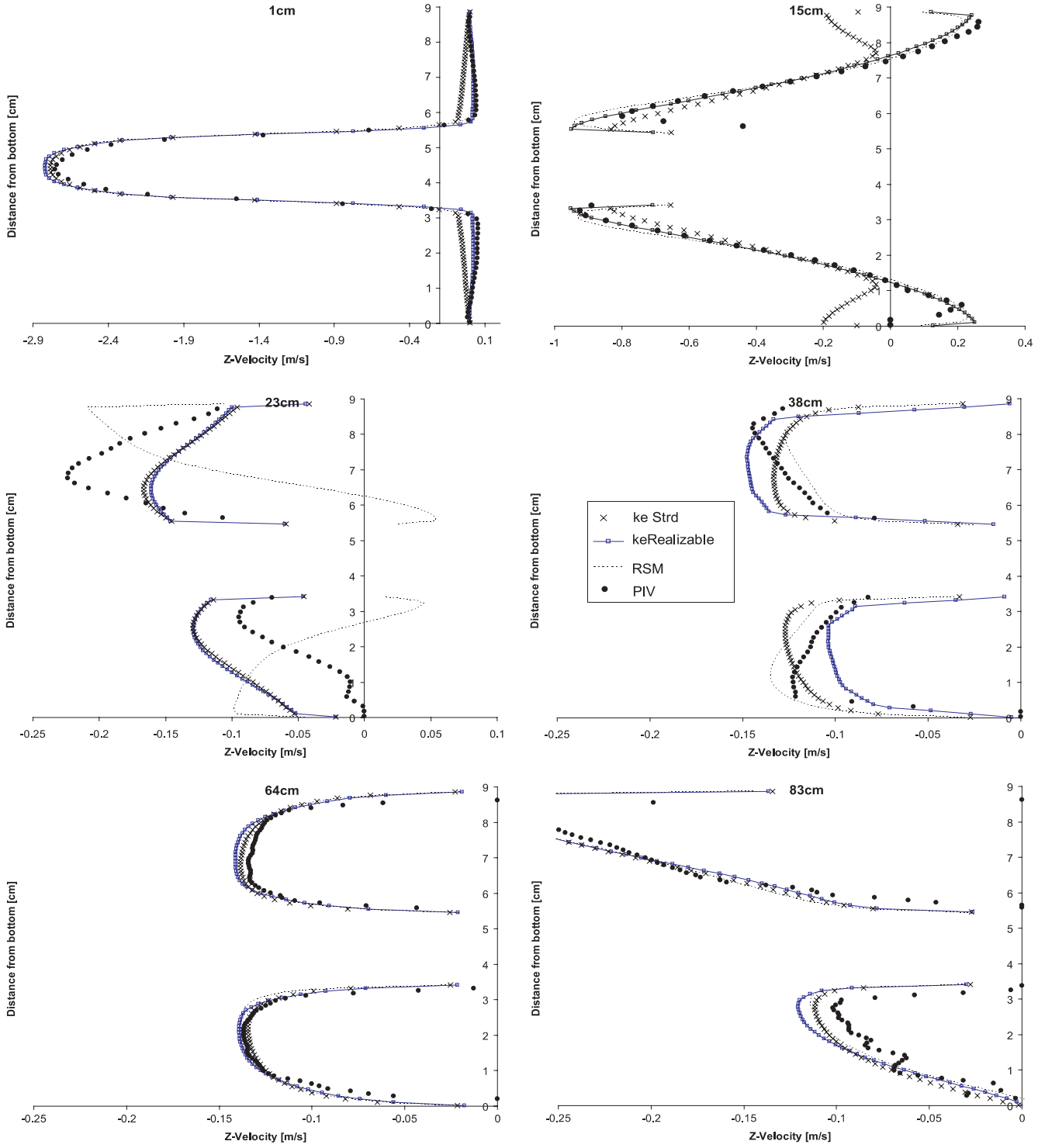

Fig. 7. z-Velocity from three turbulence models in the L-shape reactor. Comparison of model results to PIV data at different distances from the inlet.

the primary recirculation loops are not fully captured. At 23 cm, just after the lamp holder, both κ–ϵ models are in good agreement with each other and give velocity profiles comparable to that of the PIV data. Both models over-predict the flow velocity along the lower reactor side and under-predict along the top. This discrepancy might be due to the introduction of cylindrical bluff bodies (lamp holder spokes), and thus time-dependent elements, into the flow. The κ–ϵ models are not well suited to deal with anisotropic flows, and have a tendency to over-predict viscosity, and thus equalize the flow distribution over too short a distance. The z-velocity components of the RSM model after the lamp holder are non-physical and show little resemblance to the experimental data. This is likely

related to the sensitivity of this model to the unstructured mesh used in this region as discussed earlier. Finally, at 38 cm, the effects of the lamp holder are no longer prominent and all three models are in good quantitative agreement with the PIV results again. The RSM model matches the experimental flow profile closely in this region while the κ–ϵ models do not show the lower core velocity at the lamp surface. About three quarters through the reactor, at 64 cm, the flow has assumed the typical plug flow structures that are well predicted by all turbulence models. Finally, at 83 cm (6 cm from the reactor end), the flow leaving through the top exit starts to show an influence and the velocity near the top surface increases, which is captured by all the turbulence models.

A comparison of the contours of velocity magnitude obtained using the three turbulence models, with PIV experimental values in Fig. 8, shows that, in the reactor volume before the lamp holder, the predicted results of all the turbulence models agree with the PIV data and each other. At the lamp holder, the two κ–ϵ models under-predict the deflection of the jet toward the reactor wall. While the RSM model captures this flow feature, the mentioned irregularities in the unstructured mesh are also apparent. The flow deflection also explains the observed higher velocity along the outer reactor walls at 23 cm (Fig. 7).

The overall flow predictions are generally in good agreement with the experimental data throughout the reactor. The lamp holder introduces additional recirculation and mixing zones that were not accurately predicted by the κ–ϵ or the RSM models. Apart from the lamp holder region, the RSM model predicts the flow accurately; however, computational costs are approximately 60% higher than the κ–ϵ models and convergence is more problematic.

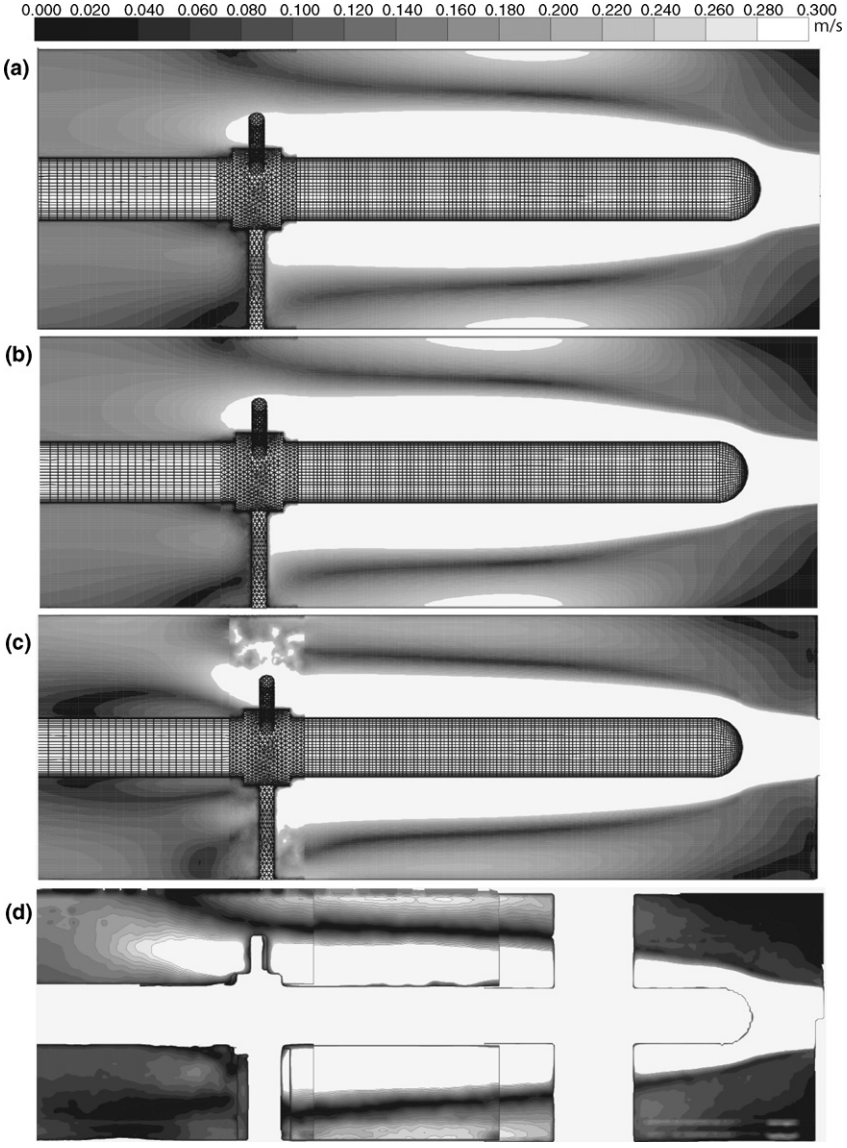

Fig. 8. Contours of velocity magnitude, center plane of the L-shape reactor. (a) Standard κ–ϵ, (b) Realizable κ–ϵ, (c) RSM and (d) PIV experimental values.

4.2. U-shape reactor

In the U-shape reactor with the inlet on top, the lamp was fixed at the inlet and a cylinder attached to the end cap was used to support the lamp at the outlet, removing the need for a lamp holder. With the exception of these structural changes, all other parameters remained fixed.

In the U-shape reactor, the flow was largely determined by the inlet jet impinging on the central annulus and the following 90 degree change of flow direction. The jet separation around the bluff body introduced a flapping motion, where the flow detaching from the lamp moved perpendicular to the main reactor axis. CFD simulations showed a similar tendency, with solutions converging towards the more stable results at either extreme of the flapping motion. The use of unstructured cells always resulted in asymmetric detaching jets and increasing the cell density only partially resolved the bias. The use of structured mesh in the inlet volume led to an almost centered secondary jet. At lower mesh densities it was noted that the secondary jet left the lamp in two streams. With increasing cells numbers this no longer occurred, even though a slight bias remained. In general, simulation results from this part of the reactor geometry were strongly influenced by both mesh structure and cell density.

A qualitative comparison of the CFD predicted symmetrical flow solution (not shown here) along the reactor's center-plane initially showed only a partial match to the PIV experimental results (Fig. 9). The inlet jet, flow structures in the inlet region, the two areas of recirculating flow to the left of the inlet, and the higher velocity along the lower reactor wall were captured. However, discrepancies were found in the upper right part of the reactor where the PIV data show returning flow structures that did not occur in the CFD results. It was found that these flow structures occurred in the CFD simulations with non-symmetrical inlet plane. The flapping flow was found to be the most likely reason; while the symmetry of the inlet plane leads to a centered flow time-averaged solution, the same does not occur along the real reactor center plane. From the lower impingement point, fast flowing layers follow the curvature of the reactor walls diagonally upwards, meeting at the top 12–14 cm along the axis. For both stable states (left and right), these flows, and thus the upper meeting point, are rotated off center to the same degree as the lower impingement point defined by the angle of the secondary jet detaching from the lamp. These two states are not laterally reversed, and the PIV results show a time average of the rotated flows. A model geometry, with structured mesh and the inlet moved off center by 1 mm, was used to emulate a similar flow by stabilizing the secondary jet on one side. CFD results for this model (Fig. 10) showed good qualitative agreement with the PIV data (Fig. 9) along the center plane.

The effects of turbulence models in the inlet region were investigated using the off-center CFD model. The z-velocity

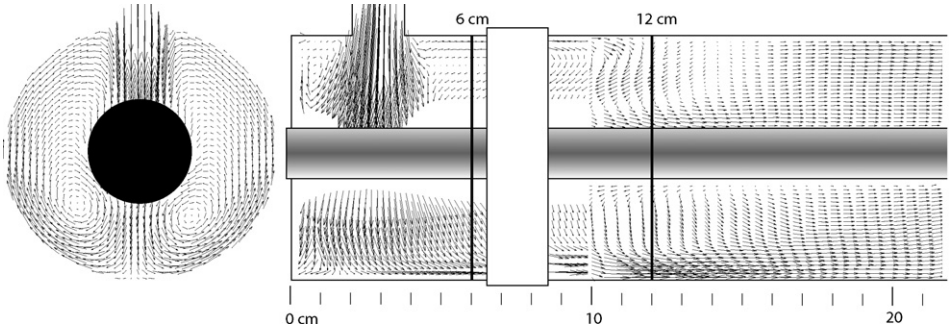

Fig. 9. Vectors of velocity magnitude from PIV experimental data for the inlet plane (left) and center plane (right) of the U-shape reactor.

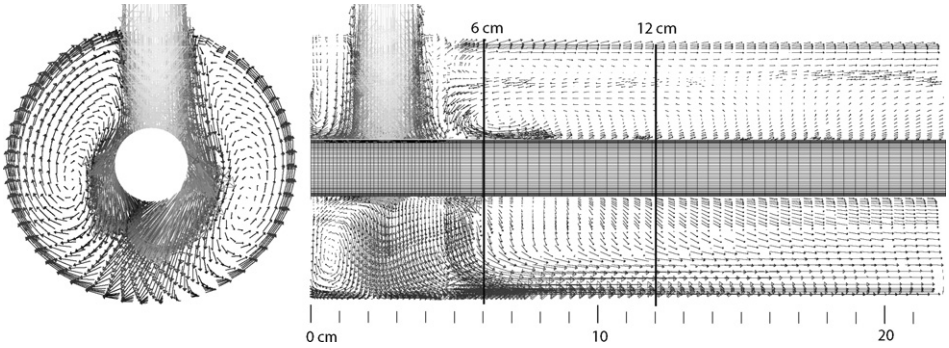

Fig. 10. Vectors of velocity magnitude on the horizontal center plane of the U-shape reactor using the Realizable κ–ϵ turbulence model. The inlet plane (left) is centered below the entrance and shows the 1 mm off-center flow stabilizing toward one side of the lamp.

components of the three tested turbulence models, and PIV data at 6, 12, and 30 cm from the reactor inlet, are shown in Fig. 11. At 6 cm, the higher flow velocity along the lower wall resulting from the secondary jet, is matched well by all turbulence models. The recirculating flow in the upper half is captured by both κ–ϵ models, while the RSM model under-predicts the velocity of the returning flow. At 12 cm, the lower reactor flow is matched relatively well by all turbulence models. In the upper reactor region, the previously described diagonal flows meet and while the RSM model gave the best match, the velocity profiles are not closely predicted by any of the turbulence models due to the time dependence of this phenomenon. This complex three-dimensional flapping turbulent flow quickly dissipates after this point. Over the following 15 cm, the annular flow velocity equalizes over the reactor's cross-section, finally assuming a plug flow character at around 30 cm, 1/3 of the distance through the reactor (Fig. 11c). The flow is then equivalent to the L-shape reactor at 64 cm (Fig. 7) and remains directly comparable right up to the outlet.

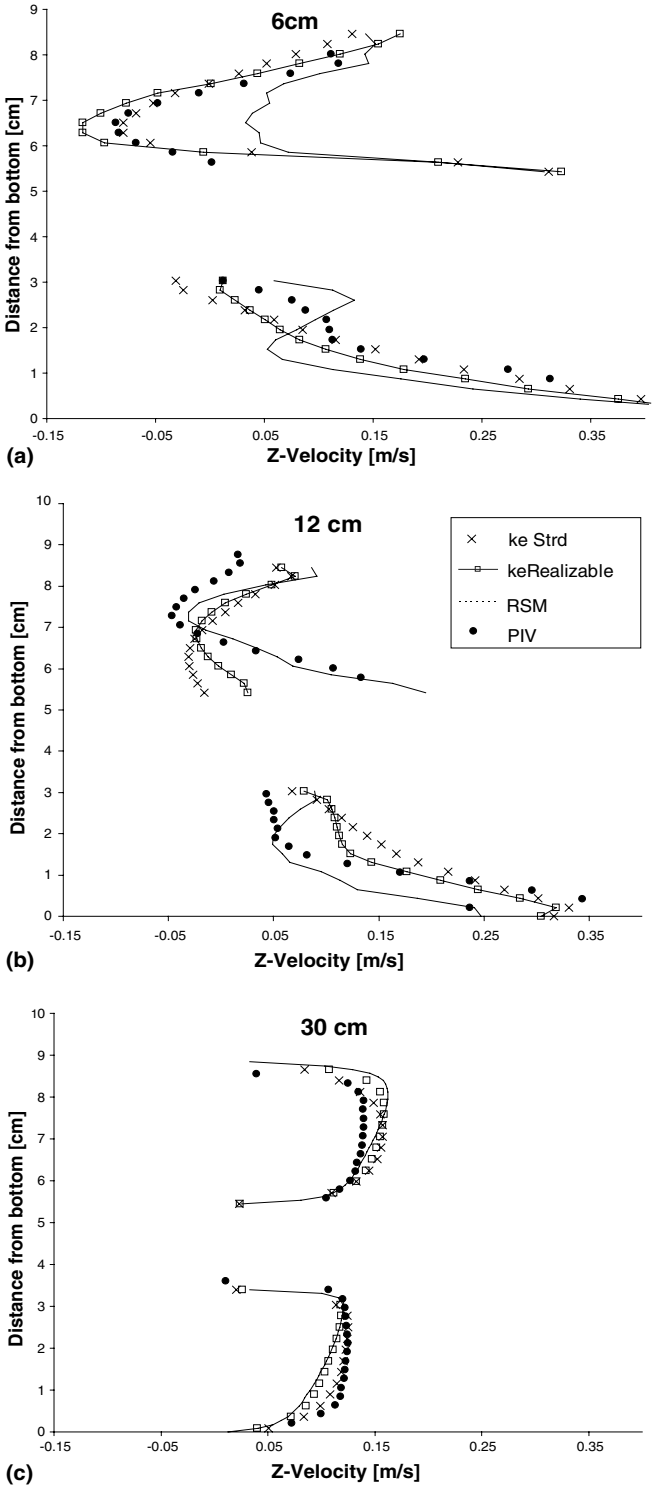

Fig. 11. z-Velocity comparison of three turbulence models to PIV results for the U-shape reactor.

5. Conclusions

The flow field of water in two reactor geometries, representing annular reactors in general, was simulated by CFD. The investigation focused on the effect of two main modeling parameters (discretisation of the volume and turbulence model) on the numerical solution for both reactor geometries and the results were compared with the experimental PIV data.

The geometry was found to have a large effect on the flow distribution in the first third of the reactor volume. The CFD flow predictions for the L-shape reactor were generally in good agreement with the PIV data, with the exception of the region immediately after the lamp holder. For the U-shape reactor, the inlet geometry with a central annulus separating the inlet jet, introduced an unstable flow resulting in a transient flapping motion that was not captured by the time-averaged CFD results. However, after a stable state of this motion was enforced by a small lateral movement of the inlet resulting in a swirling flow, the CFD simulation data closely matched the PIV findings of the same state. The instability of the fully symmetric flow was also reflected in the high mesh dependence and problematic convergence history of the numerical solutions.

It was found that objects in the reactor stream (i.e. lamp holder) need to be modeled with great care as they have a great impact on the flow field. The effects of the inlet region were no longer significant after about one-third of the reactor length for the U-shape and two-thirds for the L-shape reactor. The last third of both reactor geometries showed comparable flow structures.

The study showed that the use of structured grid not only reduced the number of cells needed for a mesh-independent solution but also reduced the influence of numerical errors. Mesh-independent solutions were achieved using over 0.5 million structured cells per reactor, corresponding to a mean cell volume of 5×10^{-9} m^3.

The effect of the two κ–ϵ and the RSM turbulence models on the final results was found to be significant in the inlet region. The Standard κ–ϵ model was not well suited for the expanding jet flows that occur in this region. While

in most regions the RSM model was somewhat superior to the Realizable κ–ϵ model, the higher mesh dependency (influence of unstructured cells) and computational cost of the former suggest the use of the later. Second-order upwind differentiation is necessary for more accurate solutions.

Overall the CFD modeling results were in good agreement with the PIV data for the L-shape reactor, and showed close agreement for the U-shape, when enough care was taken with the choice of mesh structure and turbulence model. These verified CFD models could represent the flow structure for a variety of annular reactors and could be used for UV-reactor performance simulation by integrating reaction kinetics and radiation distribution models with the CFD hydrodynamic model in the reactor.

References

Cassano, A.E., Martin, C.A., Brandi, R.J., Alfano, O.M., 1995. Photoreactor analysis and design: Fundamentals and applications. Ind. Eng. Chem. Res. 34, 2155–2201.

Chow, P., Cross, M., Pericleous, K., 1996. A natural extension of the conventional finite volume method into polygonal unstructured meshes for CFD application. Appl. Math. Modelling 20, 170–183.

Douglas, R.W., Carey, G.F., White, D.R., Hansen, G.A., Kallinderis, Y., Weatherhil, N.P., 2002. Current views on grid generation: Summaries of a panel discussion. Numer. Heat Tr. 41, 211–237.

Escudier, M.P., Smith, S., 1999. Turbulent flow of Newtonian and shear-thinning liquids through a sudden axisymmetric expansion. Exp. Fluids 27, 427–434.

Fluent, 2003. Fluent user guide: Chapter 10. Modeling turbulence. Fluent.

Hinze, J.O., 1975. Turbulence. McGraw-Hill Publishing, New York.

Hjertager, L.K., Hjertager, B.H., Solberg, T., 2002. CFD modelling of fast chemical reactions in turbulent liquid flows. Comput. Chem. Eng. 26, 507–515.

Hu, H., Kobayashi, T., Saga, T., Segawa, S., Taniguchi, N., 2000. Particle image velocimetry planar laser-induced fluoroscence measurements on lobed jet mixing flows. Exp. Fluids Suppl., 141–157.

Janex, M.L., Savoye, P., Do-Quang, Z., Blatchley, E.R., Laine, J.M., 1998. Impact of water quality and reactor hydrodynamics on wastewater disinfection by UV, use of CFD modeling for performance optimization. Water Sci. Technol. 38, 71–78.

Jaw, S.Y., Chen, C.J., 1998. Present status of second order closure turbulence models. I: Overview. J. Eng, Mech-ASCE (May), 485–501.

Kamimura, M., Furukawa, S., Hirotsuji, J., 2002. Development of a simulator for ozone/UV reactor based on CFD analysis. Water Sci. Technol. 46, 13–19.

Launder, B.E., Spalding, D.B., 1972. Lectures in mathematical models of turbulence. Academic Press, London, England.

Launder, B.E., Reece, G.J., Rodi, W., 1975. Progress in the development of a Reynolds-Stress turbulence closure. J. Fluid Mech. 68, 537–566.

Lyn, D.A., Chiu, K., Blatchley, E.R., 1999. Numerical modeling of flow and disinfection in UV disinfection channels. J. Environ. Eng. ASCE 125, 17–26.

Marchisio, D.L., Barresi, A.A., 2003. CFD simulation of mixing and reaction: The relevance of the micro-mixing model. Chem Eng Sci. 58, 3579–3587.

Meyers, K.J., Ward, R.W., Bakker, A., 1997. A digital particle image velocimetry investigation of flow field instabilities of axial flow impellers. J. Fluids Eng. 119, 623–631.

Pareek, V.K., Cox, S.J., Brungs, M.P., Young, B., Adesina, A.A., 2003. Computational fluid dynamic (CFD) simulation of a pilot-scale annular bubble column photocatalytic reactor. Chem. Eng. Sci. 58, 859–865.

Pruvost, J., Legrand, J., Legentilhomme, P., Doubliez, L., 2000. Particle image velocimetry investigation of the flow-field of a 3D turbulent annular swirling decaying flow induced by means of a tangential inlet. Exp. Fluids 29, 291–301.

Ranade, V.V., 2002. Computational flow modeling for chemical reaction engineering. Academic Press, New York.

Ranade, V.V., Perrard, M., Sauze, N.L., Xuereb, C., Bertrand, J., 2001. Trailing vortices of rushton turbines: PIV measurements and CFD simulations with snapshot approach. Trans. Chem. Eng. 79A, 3–12.

Rodi, W., 1979. Turbulence models and their application in hydraulics. IAHR Monograph, Netherlands.

Romero, R.L., Alfano, O.M., Marchetti, J.L., Cassano, A.E., 1983. Modeling and parametric sensitivity of an annular photoreactor with complex kinetics. Chem. Eng. Sci. 38, 1593–1605.

Schoenen, D., Kolch, A., Gebel, J., 1993. Influence of geometrical parameters in different irradiation vessels on UV disinfection rate. Int. J. Hyg. Env. Med. 194 (3), 313–320.

Shih, T.H., Liou, W.W., Shabbir, A., Yang, Z., Zhu, J., 1995. A new κ–ϵ eddy viscosity model for high Reynolds number turbulent flows—model development and validation. Computers Fluids 24, 227–238.

Sozzi, A., Taghipour, F., 2005. Experimental investigation of flow field in annular UV reactors using PIV. Ind. Eng. Chem. Res. 44, 9979–9988.

Unluturk, S.K., Arastoopour, H., Koutchma, T., 2004. Modeling of UV dose distribution in a thin-film UV reactor for processing of apple cider. J. Food Eng. 65 (1), 125–136.

Wright, N.G., Hargreaves, D.M., 2001. The use of CFD in the evaluation of UV treatment systems. J. Hydroinformatics 3, 59–70.